IEEE Access
Multidisciplinary | Rapid Review | Open Access Journal

Received 16 March 2023, accepted 3 May 2023, date of publication 8 May 2023, date of current version 11 May 2023.

Digital Object Identifier 10.1109/ACCESS.2023.3273783

RESEARCH ARTICLE

Design of Parameters of Fast Fourier Transform for Three-Dimensional Split Step Parabolic Equations and Mirror Kirchhoff Approximation

XIN DU, (Member, IEEE), AND JUN-ICHI TAKADA, (Senior Member, IEEE)
Department of Transdisciplinary Science and Engineering, Tokyo Institute of Technology, Tokyo 152-8550, Japan

Corresponding author: Xin Du (du.x.ab@m.titech.ac.jp)

This work was supported by the Commissioned Research through the National Institute of Information and Communications Technology (NICT), Japan, under Grant 02701.

ABSTRACT This paper proposes the simulation parameters of the fast Fourier transform (FFT) for the 3-dimensional (3D) split step parabolic equation (SSPE) and the mirror Kirchhoff approximation (MKA). The SSPE/MKA calculates the forward scattering by repeatedly applying the FFT between the space and angular spectral domains. The lacking designs for the parameters in the 3D SSPE/MKA, such as the sampling interval in the angular spectral domain, the truncation size in the space domain, and the windowing functions in the space and angular spectral domains, have motivated the establishment of the simulation parameters. The authors design the sampling interval in the angular spectral domain and the truncation size in the space domain for the 3D SSPE/MKA. In the space domain, a novel 3D windowing function combining a raised-cosine filter and the Fresnel zone number is proposed. In the angular spectral domain, the rectangular windowing function is extended to the 3D problem. The details of the proposed parameters are introduced and explained. The authors validate the proposals for a circular absorber screen and a dielectric sphere by using a reference Kirchhoff approximation (KA) and the exact solution of a dielectric sphere, respectively. Simulations are conducted by varying the object's locations, proposed parameters, and frequencies at millimeter waves and terahertz bands. The results show that the KA and 3D SSPE/MKA with the proposed parameters can present a good accuracy, which has a low root-mean-square error of less than 1 dB by comparing them with a reference KA and the exact solution, respectively. Furthermore, the parameter, which can achieve a good balance between accuracy and computational time, is designed.

INDEX TERMS Exact solution of a dielectric sphere, fast Fourier transform, forward scattering, mirror Kirchhoff approximation, split step parabolic equation, windowing function.

I. INTRODUCTION

The forward scattering is used to evaluate the radar cross sections (RCSs) in radar studies [1], [2], [3] and quantify the line-of-sight (LoS) shadowing effect in mobile communications [4]. In the beyond 5th generation (B5G) mobile communication systems, millimeter-wave (mmWave) and terahertz (THz) band radios are considered to use [5], [6], [7]. At these bands, since the human blockage significantly influences the LoS cellphone link performance, fast and accurate prediction techniques for the forward scattering are needed [8], [9].

The full-wave analysis (e.g., finite-difference time-domain (FDTD) method [10], method of moment (MoM) [11], multilevel fast multipole algorithm (MLFMA) [12], and finite element method (FEM) [13]), which discretizes and numerically solves Maxwell's equations, is an accurate calculation method that can almost reproduce the exact solutions. However, as the frequency increases, both memory consumption and calculation time increase. A high computational cost is a significant drawback for large-scale problems. On the other hand, the uniform diffraction theory (UTD) [14], [15], [16]

The associate editor coordinating the review of this manuscript and approving it for publication was Mehmet Alper Uslu.

This work is licensed under a Creative Commons Attribution-NonCommercial-NoDerivatives 4.0 License.
For more information, see https://creativecommons.org/licenses/by-nc-nd/4.0/

uses asymptotic analytic solutions for approximate calculations without solving equations, and hence it is possible to reduce memory consumption and computational complexity. However, it is difficult to handle objects with complex shapes. Therefore, a method based on physical optics approximation (PO) [17], which is an intermediate method between the full-wave analysis and UTD, is considered to be effective. In particular, the Kirchhoff approximation (KA) [18], which applies a fast Fourier transform (FFT) and an inverse FFT (IFFT) to greatly reduce the computational load while maintaining accuracy [19], [20], is used to calculate the forward scattering. In the KA calculation, the scattered field is calculated by the shadow radiation to the forward direction [21]. However, since the shadow radiation is calculated by the integration over the cross-section of the geometrical shadow region [22], the KA has difficulty evaluating the influence of the thickness on the forward scattering problem. For a thick scatterer, the mirror Kirchhoff approximation (MKA) [23], [24] based on the KA is used to predict the forward scattering by the multiple screens. Although the formulation processes are quite different, the MKA with the FFT/IFFT is mathematically the same as the split-step parabolic equation (SSPE) [25], [26], [27], [28].

The IFFT in SSPE/MKA is used to express the angular spectral domain, i.e., the superposition of plane waves with different propagation directions. Then, the FFT is used to reconstruct the electric field distributed on the desired space domain by giving the amount of the phase rotation corresponding to the propagation direction of the plane wave. A small FFT size is expected to reduce the computational cost, and it can be achieved by increasing the angular spectrum interval. The simulation parameters of the 1-dimensional (1D) FFT for the 2-dimensional (2D) SSPE/MKA was discussed in [29]. However, the work in [29] has not yet designed the parameters of the 2D FFT for the 3-dimensional (3D) problem and is a special case of a perfect electric conductor (PEC) object. On the other hand, truncation by a windowing function is required for numerical integration over an infinite space domain. In the SSPE/MKA calculation, Tukey and Hanning's windows are widely discussed for forward scattering problems [30], [31], [32], [33], [34], while they need a large truncation region resulting in a high computational cost. In the PO calculation, the windowing function based on the Fresnel zone number (FZN) [35], [36], [37] can achieve a small truncation region within an acceptable accuracy, while those works only consider the backward scattering problem. Moreover, none of the above works have designed the windowing function in the angular spectral domain. The authors previously extended the windowing function [35], [36], [37] for the forward scattering problem in the space domain and have properly proposed the windowing function in the angular spectral domain [29]. However, those windowing functions are only considered for the 2D problem.

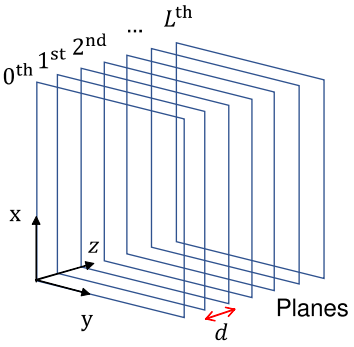

FIGURE 1. Model of the 3D SSPE/MKA.

This paper aims to design the simulation parameters of the 2D FFT, which is applied to calculate the forward scattering by a 3D dielectric object. This paper designs the sampling interval in the angular spectral domain as well as the truncation size in the space domain for the 3D SSPE/MKA. In the space domain, the novel windowing function based on FZN is proposed. In the angular spectral domain, the rectangular windowing function is extended to the 3D problem. The validation of the proposal is considered in two steps. In the first step, the simulation of the KA using the proposed parameters of the 2D FFT is compared by the reference KA, which does not use the proposed parameters but only works for the forward scattering by an arbitrarily shaped screen. The purpose of the first step is to confirm the validity of the proposed parameters. In the second step, the simulation of the SSPE/MKA with the proposed parameters is compared by using the exact solution of a dielectric sphere. The second step aims to validate the accuracy of the SSPE/MKA with the proposed parameters for an arbitrarily shaped 3D object.

The remainder of this paper is organized as follows. The design of simulation parameters (i.e., the sampling interval in the angular spectral domain, the truncation size in the space domain, and the windowing functions in the space and angular spectral domains) for the 3D SSPE/MKA is explained in Section II. Section III presents and discusses the simulation environment, simulation conditions, simulation parameters, simulation methods, and results for validating the proposed parameters. The simulation and results for validating the 3D SSPE/MKA with the proposed parameters are shown in Section IV. Finally, a conclusion of this work is given in Section V.

II. DESIGN OF SIMULATION PARAMETERS FOR 3D SSPE/MKA

This section proposes the design of the simulation parameters for the 3D SSPE/MKA. The simulation parameters include the sampling interval in the angular spectral domain, the truncation size in the space domain, and the windowing functions in the space and angular spectral domains.

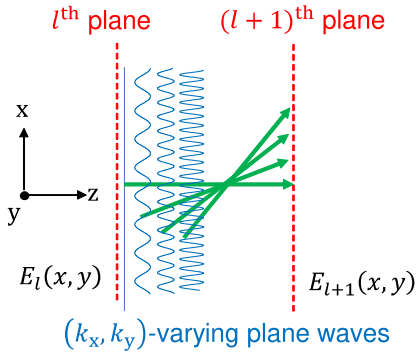

FIGURE 2. Plane wave decomposition by FT and IFT.

A. SAMPLING INTERVAL IN ANGULAR SPECTRAL DOMAIN AND TRUNCATION SIZE IN SPACE DOMAIN

The model of SSPE/MKA can be seen as slices of the 3D space by multiple planes, as shown in Fig. 1 d is the distance between two planes and can be determined in [25] and [29]db@MKA3 . The 3D SSPE/MKA applies a 2D inverse Fourier transformation (IFT) and a 2D Fourier transformation (FT) to evaluate the propagation between two parallel planes $z = ld$ and $z = (l+1)d$ by (1)-(3).

$$\tilde{E}_l(k_x, k_y) = \int_{-\infty}^{\infty}\int_{-\infty}^{\infty} E_l(x,y)e^{j(k_x x+k_y y)}dxdy \tag{1}$$

$$E_{l+1}(x,y) = \frac{1}{4\pi^2}\int_{-\infty}^{\infty}\int_{-\infty}^{\infty}\tilde{E}_l(k_x,k_y) \cdot e^{-j(k_x x+k_y y+k_z d)}dk_x dk_y \tag{2}$$

$$k_z = \begin{cases} +\sqrt{k_0^2-k_x^2-k_y^2} & (k_x^2+k_y^2 \le k_0^2) \\ -j\sqrt{k_x^2+k_y^2-k_0^2} & (k_x^2+k_y^2 > k_0^2) \end{cases} \tag{3}$$

where x and y are the parameters of the x-space and y-space domains, respectively. k_x, k_y, and k_z are the parameters of the angular spectral domains corresponding to the x-space, y-space, and z-space domains, respectively. k_0 is the free-space wave number. $E_l(\cdot)$ is the total scalar electric field in the l^{th} plane $z = ld$ ($l = 0, 1, \ldots, L$). $\tilde{E}_l(\cdot)$ is the 2D IFT of E_l. The cases of $k_x^2 + k_y^2 \le k_0^2$ and $k_x^2 + k_y^2 > k_0^2$ in (3) represent the propagation and evanescent waves, respectively.

The 2D IFT in (1) decomposes the source field E_l as (k_x, k_y)-varying plane waves with a complex amplitude of $\tilde{E}_l$. Then, the 2D FT in (2) reconstructs the field E_{l+1} in the next plane by giving the amounts of the phase rotations corresponding to the propagation directions of those plane waves, as shown in Fig. 2. Evanescent waves exist in those plane waves with $k_x^2 + k_y^2 > k_0^2$, since the complex exponential factor $e^{-jk_z d}$ becomes the decay exponential factor $e^{-\sqrt{k_x^2+k_y^2-k_0^2}d}$, according to (3). It is known as an evanescent wave where the energy is not transferred but decays exponentially. Usually, the calculation ignores the evanescent wave when d is large [38]. By repeatedly applying 2D IFT/FT among those planes, the desired fields can be calculated finally.

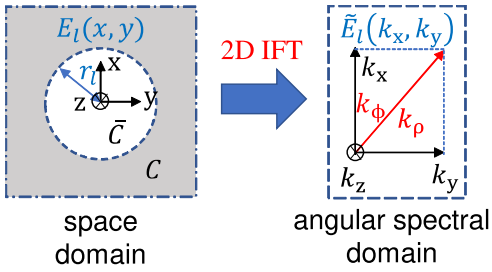

FIGURE 3. Parameters in the space and angular spectral domains.

For calculating the 2D IFT/FT fast, the 2D IFFT/FFT is applied. Therefore, discretization for the numerical calculation is needed in the space and angular spectral domains. Normally, $\lambda/10$ is widely used to represent the sampling interval in the space domain as a rule of thumb for accuracy, where λ is a wavelength in the free space [23]. The meaning of the $\lambda/10$ sampling criterion is that there are at least ten sampling points in one phase period (one cycle of phase rotation), which is sufficient. Previous work in [29] proposed the sampling interval in the angular spectral domain for the 2D SSPE/MKA by considering that the phase period in the angular spectral domain at the major-contribution regions should be sufficiently sampled. The major-contribution regions for the 2D problem are the left and right edges of the shadowing object. The designed sampling interval in the angular spectral domain is determined by the maximum value of the distance from each edge to the phase center, which is the projecting point of the antenna onto the plane. Previous works only designed the parameters of the 1D FFT for the 2D SSPE/MKA, and hence the parameters of the 2D FFT for the 3D problem are needed. However, the 3D problem has a continuous edge of the shadowing object that cannot be separated to the left and right.

This work considers that the maximum value of the distance from each edge to the phase center should be extended to the radius of the maximum circle, which has a center of the phase center and includes the whole boundary of the shadowing object. The proposal for designing the sampling interval in the angular spectral domain for the 3D MKA is similar to the 2D MKA. To accurately integrate (2) numerically, the phase period of $\tilde{E}_l(k_x, k_y)e^{-j(k_x x+k_y y+k_z d)}$ should be sufficiently sampled.

Firstly, the phase period of $\tilde{E}_l(k_x, k_y)$ alone is calculated. For the sake of simplicity, a uniform plane wave upon the l^{th} plane is assumed. Through the KA, the total fields distributed on the l^{th} plane in the lit and shadowed regions can be approximated as the incident field E_l^{i} and zero, respectively. Viz.

$$E_l(x,y) \approx \begin{cases} E_l^{\text{i}} & ((x,y) \in C) \\ 0 & ((x,y) \in \bar{C}) \end{cases} \tag{4}$$

where regions $\bar{C}$ and C are the inside and outside of the maximum circle, respectively, as shown in Fig. 3. Substituting

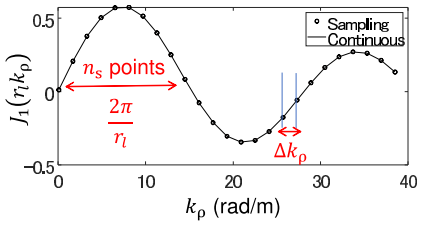

FIGURE 4. The plot of $J_1(r_l k_\rho)$ with the value of $r_l = 0.25$ m [29].

(4) into (1), the $\tilde{E}_l(k_x, k_y)$ is calculated as

$$\tilde{E}_l(k_x, k_y) \approx \iint_C E_l^i e^{j(k_x x + k_y y)} dx dy = 2\pi E_l^i r_a \frac{J_1(r_l k_\rho)}{k_\rho} \tag{5}$$

where r_l is the radius of the maximum circle in the l^{th} plane and $k_\rho = \sqrt{k_x^2 + k_y^2}$. $J_1(\cdot)$ is the Bessel function of the first kind for the first order. The derivation of (5) is shown in Appendix A. From the factor of $J_1(r_l k_\rho)$ in (5), the phase period of $\tilde{E}_l(k_x, k_y)$ can be calculated as $2\pi/r_l$ in the k_ρ-angular spectral domain.

Secondly, the phase period of $e^{-j(k_x x + k_y y + k_z d)}$ should also be evaluated. However, the factor of $e^{-j(k_x x + k_y y + k_z d)}$ does not determine the phase period at the major contribution region, and the reason is explained as follows. From the factor of $1/k_\rho$ in (5), it can be determined that $(k_x, k_y) = (0, 0)$ is the pole of $\tilde{E}_l(k_x, k_y)e^{-j(k_x x + k_y y + k_z d)}$, which makes a significant contribution to the integral. In the major contribution region, the factor of $e^{-j(k_x x + k_y y + k_z d)}$ reduces to a constant of $e^{-jk_0 d}$ due to $(k_x, k_y, k_z) = (0, 0, k_0)$. Therefore, the key factor determining the phase period of $\tilde{E}_l(k_x, k_y)e^{-j(k_x x + k_y y + k_z d)}$ at the major contribution region is $J_1(r_l k_\rho)$ alone.

As shown in Fig. 4, the phase period of $J_1(r_l k_\rho)$ is proposed to be sufficiently sampled by at least n_s points as

$$\frac{2\pi}{r_l} = n_s \Delta k_\rho \tag{6}$$

where Δk_ρ is the sampling interval in the k_ρ-angular spectral domain. Especially, $n_s = 10$ corresponds to the $\lambda/10$ sampling criterion in the space domain.

Let Δk_x and Δk_y be the sampling intervals in the k_x-angular spectral and k_y-angular spectral domains, respectively, and suppose that they have the same value. The total derivative of k_ρ is applied as

$$\Delta k_\rho = \cos k_\phi \Delta k_x + \sin k_\phi \Delta k_y \le \sqrt{2}\Delta k_x \tag{7}$$

where $\cos k_\phi = k_x/k_\rho$ and $\sin k_\phi = k_y/k_\rho$.

Using (6) and (7), the sampling interval in the k_x-angular spectral domain is designed by taking the minimum value for the accuracy of each plane as

$$\Delta k_x = \min_l \frac{\sqrt{2}\pi}{n_s r_l} \tag{8}$$

Suppose that the truncation sizes of the x-space and y-space domains have the same value of X, which can be derived as

$$X = \frac{2\pi}{\Delta k_x} = \max_l \sqrt{2} n_s r_l \tag{9}$$

B. WINDOWING FUNCTION IN SPACE DOMAIN

Since the numerical integral cannot deal with the infinite large plane, truncation to a finite large plane is needed. The regions far away from the edges and phase center (i.e., the projecting point of the antenna onto the plane), where the integral of the rapidly oscillating function $E_l(x, y)e^{j(k_x x + k_y y)}$ does not contribute to the final integral due to the cancellation, can be truncated. However, when truncated as it is in a finite range, the fictitious diffracted waves are generated due to the discontinuity of the electric field at the boundary of the truncation region. Therefore, for avoiding those discontinuities, it is necessary to apply the windowing function to the electric field at the boundary of the truncation region to gradually approach zero.

The authors previously applied the windowing function based on FZN for a 2D forward scattering problem [29]. Assuming that the shadowing screen with the width of w is parallel to the x-axis, the 2D spatial windowing function $W_{2D}^{Sp}(\cdot)$ is introduced as

$$W_{2D}^{Sp}(x) = \begin{cases} \frac{1}{2}\left\{\cos\left(\frac{n_F(x) - n_F(s)}{n_F(a) - n_F(s)}\pi\right) + 1\right\} & (|x - s| \le a) \\ 0 & (|x - s| > a) \end{cases} \tag{10}$$

$$n_F(x) = \frac{\sqrt{x^2 + b^2} + \sqrt{x^2 + c^2} - (b + c)}{\frac{\lambda}{2}} \tag{11}$$

where $n_F(\cdot)$ is the number of the Fresnel zone. a is the absolute value of the x-coordinate corresponding to the boundary of the 2D spatial windowing function, and its determination is shown in [36] and [29]. b and c are the distances from the screen to the transmitter (Tx) and receiver (Rx), respectively. s is the x-coordinate of the stationary phase point (SPP) or edge point (EP), which makes a significant contribution to the incidence or diffraction, respectively. For the non-line-of-sight (NLoS) problem, where the phase center is shadowed, the SPP/EPs are considered as two edge points of the screen. For the line-of-sight (LoS) problem, where the phase center is not shadowed, the SPP/EPs are considered as an edge point of the screen and a phase center [23]. Since the values of the fields making a significant contribution should keep intact, the windowed values of the SPP/EPs should be set to unity, as shown in Fig. 5. Figures 5a and 5b show examples of the plots of the 2D spatial windowing functions for the NLoS and LoS problems, respectively, with the values of $w = 0.5$ m, $b = 2$ m, $c = 8$ m, and $\lambda = 4.5$ mm [29]. For the plane wave incidence, the number of the Fresnel zone is calculated by assuming that the Tx is placed at infinity as

$$\lim_{b \to \infty} n_F(x) = \frac{\sqrt{x^2 + c^2} - c}{\frac{\lambda}{2}} \tag{12}$$

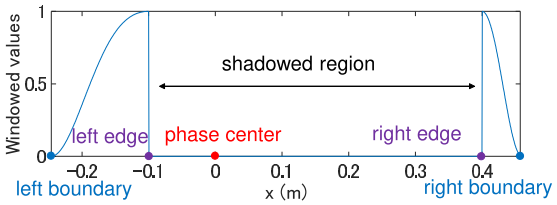

(a) NLoS condition.

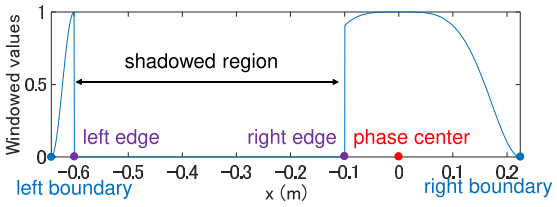

(b) LoS condition.

FIGURE 5. The 2D spatial windowing function.

The above work applies two windowing functions to the left and right sides of the x-axis, respectively, for the 2D problem. It works well since the shadowed region isolates two windowing functions to avoid interference. However, for the 3D problem mentioned in Section II, a continuous edge of the shadowed region cannot be separated to the left and right. All the points of that continuous edge are considered as the SPP/EPs, and hence the windowed values at those points should be set to unity. A single windowing function of $W_{\mathrm{2D}}^{\mathrm{Sp}}(\cdot)$ can only work when the shape of the shadowed region is a circle with the center of the phase center. In the other case (e.g., the center of the shadowed region is not the phase center), there is a need to take multiple windowing functions to let the windowed values at the edge as unity. However, if multiple windowing functions are applied, the interference of those windows will occur due to the continuity of the edge of the shadowed region. Therefore, a new 3D spatial windowing function is needed to overcome the above challenges. In this work, the 3D spatial windowing function is proposed as

$$W_{\mathrm{3D}}^{\mathrm{Sp}}(\boldsymbol{\rho}) = \begin{cases} 1 & (\boldsymbol{\rho} \in B) \\ \dfrac{1}{2}\left\{\cos\left(\dfrac{n_{\mathrm{F}}(\boldsymbol{\rho}) - n_{\mathrm{F}}(\boldsymbol{s})}{n_{\mathrm{F}}(\boldsymbol{a}) - n_{\mathrm{F}}(\boldsymbol{s})}\pi\right) + 1\right\} & (\boldsymbol{\rho} \in C) \\ 0 & (\boldsymbol{\rho} \in A, D) \end{cases} \tag{13}$$

where $\boldsymbol{\rho}$ is the position vector of the arbitrary point in the x-y plane, i.e., $\boldsymbol{\rho} = (x, y)$. $W_{\mathrm{3D}}^{\mathrm{Sp}}(\cdot)$ is the 3D spatial windowing function, which is proposed as a raised-cosine filter based on FZN. Especially, the previous windowing function $W_{\mathrm{2D}}^{\mathrm{Sp}}(\cdot)$ can also be seen as a raised-cosine filter with a roll-off factor of 1. The proposed windowing function $W_{\mathrm{3D}}^{\mathrm{Sp}}(\cdot)$ can be considered as the extension of $W_{\mathrm{2D}}^{\mathrm{Sp}}(\cdot)$ with a general roll-off factor. Figure 6a shows an example of the plot of the 3D spatial windowing function with the values of $r_l = 0.2$ m, $b = 2$ m, $c = 8$ m, $\lambda = 4.5$ mm, and $n_{\mathrm{s}} = 10$. Figure 6b is the top view of Fig. 6a. As shown in Fig. 6b, there are four regions in the x-y plane, i.e., A, B, C, and D. Region A can be an arbitrarily shaped shadowed region. The phase

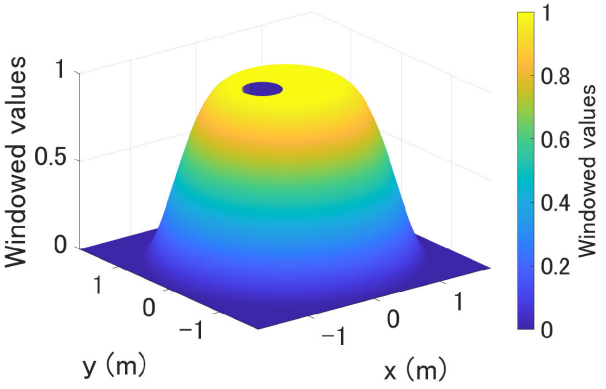

(a) Proposed windowing function.

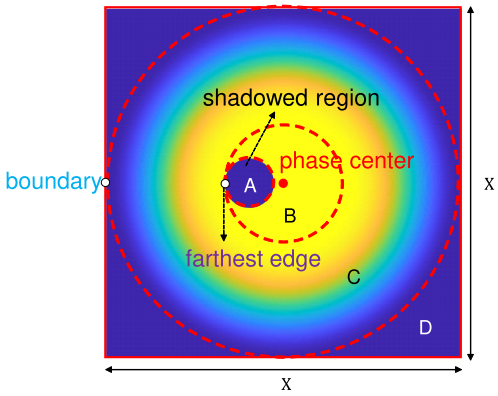

(b) Four regions in the x-y plane.

FIGURE 6. The 3D spatial windowing function.

center can be at an arbitrary position, even outside of region A. The windowed value of region A is set to zero due to the assumption of the KA. Region B is determined by a circle whose size corresponds to the farthest edge of region A from the phase center. $\boldsymbol{s}$ is the position vector of the farthest edge. The windowed value of region B is set to unity to ensure that the values of the fields at the edges and phase center keep intact. Region C is determined by a circle whose size corresponds to the value of X proposed in Section II. $\boldsymbol{a}$ is the position vector of the boundary of the window, i.e., $2|\boldsymbol{a}| = X$. The windowing function in region C is a cosine function to gradually approach zero for avoiding the discontinuity of the fields at the boundary. Region D is outside of region C. The windowed value of region D is set to zero due to the truncation.

C. WINDOWING FUNCTION IN ANGULAR SPECTRAL DOMAIN

Although the factor of $e^{-\mathrm{j}(k_{\mathrm{x}}x+k_{\mathrm{y}}y+k_{\mathrm{z}}d)}$ does not determine the phase period at the major contribution region according to Section II, it dominates the phase period with an increase in k_ρ. The factor of $e^{-\mathrm{j}k_{\mathrm{z}}d}$ around $k_\rho \simeq 0$ can be approximated by applying the Fresnel region approximation [39] as

$$e^{-\mathrm{j}k_{\mathrm{z}}d} = e^{-\mathrm{j}\sqrt{k_0^2 - k_\rho^2}d} \approx e^{\mathrm{j}\left(\frac{d}{2k_0}k_\rho^2 - k_0 d\right)} \tag{14}$$

Thus, the phase function $\phi(\cdot)$ of $e^{-\mathrm{j}k_z d}$ can be considered as

$$\phi(k_\rho) \sim \frac{d}{2k_0}k_\rho^2 \tag{15}$$

Therefore, the phase of $e^{-\mathrm{j}k_z d}$ is approximately k_ρ^2-dependent, which has a decreasing phase period with an increase in k_ρ, as shown in Fig. 7a. Figure 7b shows the behavior of $e^{-\mathrm{j}k_z d}$ around $k_\rho \simeq k_0$. We can find that the wave is evanescent when k_ρ is larger than the wave number.

There is a vast discretization error when the equally sampled points face a decreasing phase period. The region far away from the major contribution region, where the integral of the oscillating function does not contribute to the final integral, can be truncated. Those regions can be numerically integrated with vain if the number of samples per phase period is sufficiently large, e.g., at least 2 sampling points per phase period according to the Nyquist sampling criterion [29]. However, the proposed interval in the phase period far away from the major contribution region may not provide sufficient sampling points due to a decreasing phase period with an increase in k_ρ. The numerical integration of the vanishing region is erroneous when the number of samples per phase period is insufficiently small. Therefore, it is better to truncate rather than inaccurately integrate the region numerically.

In case of a small propagating distance d, there is no need to consider the extra discretization error, since $\tilde{E}_l(k_\mathrm{x}, k_\mathrm{y})e^{-\mathrm{j}(k_\mathrm{x}x+k_\mathrm{y}y+k_z d)}$ is dominated by $\tilde{E}_l(k_\mathrm{x}, k_\mathrm{y})$, which has a constant phase period with the size of $2\pi/r_l$. However, in case of a large propagating distance d, there is a need to take the windowing function for reducing the extra discretization error, since $\tilde{E}_l(k_\mathrm{x}, k_\mathrm{y})e^{-\mathrm{j}(k_\mathrm{x}x+k_\mathrm{y}y+k_z d)}$ is dominated by $e^{-\mathrm{j}k_z d}$, which has a decreasing phase period. In the previous work [29] for the 2D problem, the rectangular windowing function $W_{\mathrm{2D}}^{\mathrm{An}}(\cdot)$ was introduced for the truncation in the k_x-angular spectral domain as

$$W_{\mathrm{2D}}^{\mathrm{An}}(k_\mathrm{x}) = \begin{cases} 1 & (|k_\mathrm{x}| \le k_\mathrm{w}) \\ 0 & (|k_\mathrm{x}| > k_\mathrm{w}) \end{cases} \tag{16}$$

where k_w is the size of the rectangular window, and its formulation is explained in [29]. Figure 8 shows an example of the plot of the 2D angular spectral windowing function with the values of $k_0 = 1394$ rad/m, $w = 0.5$ m, and $d = 8$ m [29].

The above work considers the windowing function in the k_x-angular spectral domain, since the phase function has a decreasing phase period with an increase in $|k_\mathrm{x}|$ [29]. However, in this work, the phase period decreases with an increase in k_ρ. Therefore, this work proposes the rectangular windowing function in the k_ρ-angular spectral domain for the 3D problem as

$$W_{\mathrm{3D}}^{\mathrm{An}}(\boldsymbol{k}_\rho) = \begin{cases} 1 & (k_\rho \le k'_\mathrm{w}) \\ 0 & (k_\rho > k'_\mathrm{w}) \end{cases} \tag{17}$$

where $\boldsymbol{k}_\rho$ is the position vector of the arbitrary point in the k_x-k_y plane, i.e., $\boldsymbol{k}_\rho = (k_\mathrm{x}, k_\mathrm{y})$. $W_{\mathrm{3D}}^{\mathrm{An}}(\cdot)$ is the rectangular windowing function in the k_ρ-angular spectral domain, but the circular cylindrical windowing function in the k_x-k_y coordinate system. k'_w is the radius of a circular cylindrical window. The rectangular windowing function is chosen because the envelope of $\tilde{E}_l(k_\mathrm{x}, k_\mathrm{y})e^{-\mathrm{j}(k_\mathrm{x}x+k_\mathrm{y}y+k_z d)}$ decays fast due to the factor of $1/k_\rho$ in (5). Thus, the rectangular windowing function results in a negligibly small truncation error [29]. By proposing that the regions unsatisfying the Nyquist sampling criterion should be truncated, the size of k'_w is determined by using (6) and (15) as

$$\phi(k'_\mathrm{w}) - \phi(k'_\mathrm{w} - n_\mathrm{c}\Delta k_\rho) = 2\pi \tag{18a}$$

$$\Rightarrow k'_\mathrm{w} = \max_l \frac{n_\mathrm{s} k_0 r_l}{n_\mathrm{c} d} \tag{18b}$$

where n_c is the Nyquist sampling number, i.e., 2 [29]. Figure 9 shows an example of the plot of the 3D angular spectral windowing function with the values of $k_0 = 1394$ rad/m $r_l = 0.2$ m, $d = 8$ m, and $n_\mathrm{s} = 10$.

III. VALIDATION OF PROPOSED PARAMETERS

The proposed parameters are validated by comparison with the reference KA. The details of the reference KA are explained in Appendix B. As explained in Appendix B, the reference KA can calculate the shadow radiation from a finite region in (30)-(31), and hence truncation by the windowing function is not needed. Moreover, since the scattered field can be determined by the vector potentials, there is no need to apply the 2D FFT. Therefore, the reference KA does not use the proposed parameters of this work, and hence it can be considered as a reference to validate the KA with the proposed parameters.

Since the reference KA can only deal with an arbitrarily shaped screen, a circular absorber screen is considered as the shadowing object. As shown in Fig. 10, the phase center, which is the projecting point of the Rx onto the screen, is set as the coordinate origin. A circular absorber screen placed in the plane $z = 0$ is moving along the y-axis. A uniform plane wave traveling along the z-axis is a normal incidence on the screen. The Rx is assumed with the same height (i.e., x-value) as the center of the circular screen. r_0 denotes the radius of the circular screen. f denotes the frequency. d_1 denotes the distance between the center of the circular screen and the phase center. d_2 denotes the distance between the phase center and the Rx.

Table 1 shows the simulation parameters for a circular absorber screen. Four frequencies are considered at mmWave/THz bands, i.e., 40 GHz, 60 GHz, 80 GHz, and 100 GHz. Considering the human-size shadowing problem, r_0 is set to 0.2 m. The key parameter n_s, which deter-

TABLE 1. Simulation parameters for a circular absorber screen.

Parameters	Values
f (GHz)	40, 60, 80, 100
r_0 (m)	0.2
d_1 (m)	$[0, 0.4]$
d_2 (m)	8
n_s	2, 4, 6, 8, 10
n_c	2
Δx (λ)	0.1

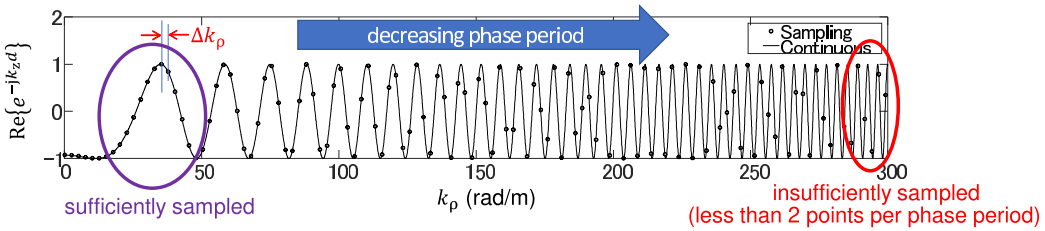

(a) The behavior of $e^{-\mathrm{j}k_z d}$ around $k_\rho \simeq 0$.

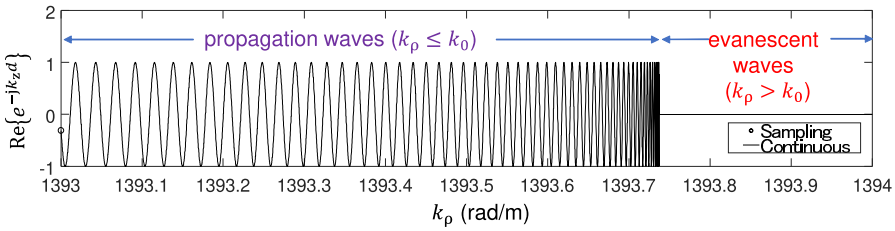

(b) The behavior of $e\_^{\mathrm{j}k_z d}$ around $k_\rho \simeq k_0$.

FIGURE 7. The plot of the real part of $e^{-\mathrm{j}k_z d}$ with the values of $k_0 = 1394$ rad/m and $d = 8$ m [29].

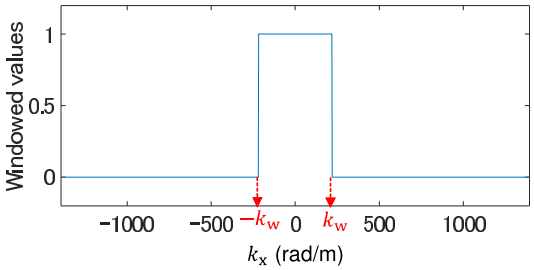

FIGURE 8. The 2D angular spectral windowing function.

mines the sampling interval in the angular spectral domain, the size of the windowing functions in the space domain, and the truncation region in the angular spectral domain, is varied from 2 to 10 with an interval of 2. n_s needs to be an even number because the number of the sampling points distributed on $[0, \pi]$ and $[\pi, 2\pi]$ should be the same in one cycle of phase rotation. The spatial interval Δx is set to 0.1λ for accuracy.

The processor of the calculating computer is an Intel(R) Core(TM) i9-12900K CPU @ 3.19 GHz. The usable installed memory of the calculating computer is 63.7 GB. The system type of the calculating computer is a 64-bit operating system with an x64-based processor. The simulation software is MATLAB.

Figures 11a-11d show the plots of the shadowing gain, which is the total field normalized by an incident field, at 40 GHz, 60 GHz, 80 GHz, and 100 GHz, respectively. For each frequency band, both perpendicular polarization (perp.) and parallel polarization (para.) are simulated for the reference KA. Although the KA based on a FFT (FFT KA) can not deal with the boundary conditions (i.e., the surface impedance and the polarization), those contributions are smaller than the shadowed FZN at a high frequency [40]. d_1 is varied from 0 to 0.4 m with an interval of 0.002 m, and hence each figure has 200 tests. The results show that the KA with the proposed parameter $n_s \ge 4$ is a good agreement with the reference KA. Considering the reference KA as a reference, the authors calculate the root-mean-square error (RMSE) as

$$\mathrm{RMSE} = \sqrt{\sum_{j=1}^{m} \frac{\left(\mathrm{SG}_j^{\mathrm{Pro}} - \mathrm{SG}_j^{\mathrm{Ref}}\right)^2}{m}} \tag{19}$$

where $\mathrm{SG}_j^{\mathrm{Ref}}$ is the shadowing gain calculated by the reference KA on a dB scale for the j^{th} test, and $\mathrm{SG}_j^{\mathrm{Pro}}$ is the shadowing gain calculated by the KA with the proposed parameter on a dB scale for the j^{th} test. m is the total number of tests per figure (i.e., $m = 200$). The RMSEs at all the frequencies, polarization, and n_s-values are summarized in Table 2.

The results show that the KA with the proposed parameter $n_s \ge 4$ achieves a good accuracy with a low root-mean-square error of less than 1 dB, compared with the reference KA. Therefore, the validity of the proposed parameters is confirmed for the KA calculation. The computational time of the FFT KA at all the frequencies and n_s-values are summarized in Table 3. From Table 3, it can be found that the proposed parameter $n_s = 4$ can achieve a lower computational time of 0.2 s – 12.3 s within an acceptable accuracy, compared with the other n_s-values.

IV. VALIDATION OF 3D SSPE/MKA WITH PROPOSED PARAMETERS

The 3D SSPE/MKA with the proposed parameters for an arbitrarily shaped 3D object is validated by comparison with the exact solution of the scattering by a lossy dielectric sphere. The details of the exact solution of the scattering by a lossy dielectric sphere are explained in Appendix C.

As shown in Fig. 12, a dielectric sphere with the center in the plane $z = 0$ is moving along the y-axis. A uniform plane wave traveling along the z-axis is a normal incidence on the

TABLE 2. Summary of the RMSEs at different frequencies, polarization, and n_s-values for a circular absorber screen.

Frequencies (polarization)	RMSEs at $n_s = 2$	RMSEs at $n_s = 4$	RMSEs at $n_s = 6$	RMSEs at $n_s = 8$	RMSEs at $n_s = 10$
40 GHz (perp.)	3.93 dB	0.33 dB	0.08 dB	0.05 dB	0.04 dB
40 GHz (para.)	3.93 dB	0.33 dB	0.08 dB	0.05 dB	0.04 dB
60 GHz (perp.)	1.62 dB	0.17 dB	0.06 dB	0.04 dB	0.02 dB
60 GHz (para.)	1.61 dB	0.17 dB	0.06 dB	0.04 dB	0.03 dB
80 GHz (perp.)	1.34 dB	0.18 dB	0.07 dB	0.04 dB	0.03 dB
80 GHz (para.)	1.35 dB	0.18 dB	0.07 dB	0.04 dB	0.03 dB
100 GHz (perp.)	0.66 dB	0.18 dB	0.06 dB	0.03 dB	0.03 dB
100 GHz (para.)	0.67 dB	0.19 dB	0.06 dB	0.04 dB	0.03 dB

TABLE 3. Summary of the computational time (Cal. time) of the FFT KA at different frequencies and n_s-values for a circular absorber screen.

Frequencies	Cal. time at $n_s = 2$	Cal. time at $n_s = 4$	Cal. time at $n_s = 6$	Cal. time at $n_s = 8$	Cal. time at $n_s = 10$
40 GHz	0.1 s – 0.5 s	0.2 s – 2.0 s	0.5 s – 4.3 s	0.8 s – 8.0 s	1.3 s – 12.4 s
60 GHz	0.1 s – 1.1 s	0.5 s – 4.4 s	1.1 s – 10.2 s	2.0 s – 18.5 s	3.0 s – 29.4 s
80 GHz	0.2 s – 2.0 s	0.9 s – 8.1 s	2.0 s – 18.5 s	3.4 s – 34.3 s	5.5 s – 56.5 s
100 GHz	0.3 s – 3.1 s	1.3 s – 12.3 s	3.0 s – 29.5 s	5.5 s – 56.6 s	8.7 s – 166.1 s

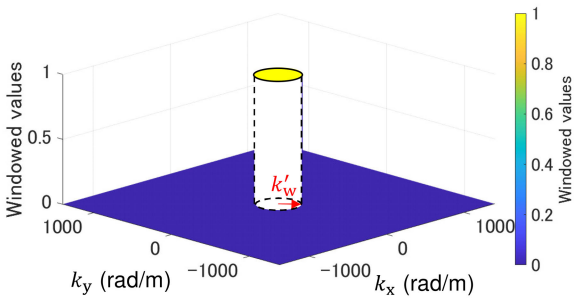

(a) Rectangular coordinate system.

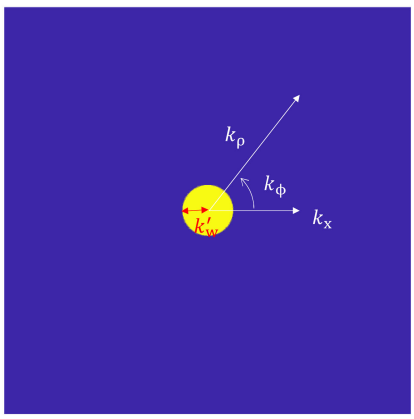

(b) Cylindrical coordinate system.

FIGURE 9. The 3D angular spectral windowing function.

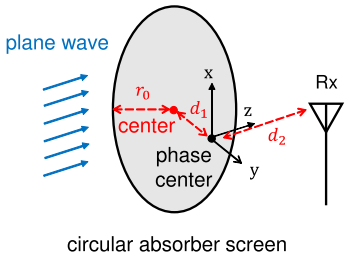

FIGURE 10. Simulation environment for a circular absorber screen.

TABLE 4. Simulation parameters for a circular absorber screen.

Parameters	Values
f (GHz)	40, 60, 80, 100
$\dot{\epsilon}_r$	$11.7 - j14.3$, $8.0 - j10.9$, $6.4 - j8.6$, $5.6 - j7.1$
R (m)	0.2
d_1 (m)	$[0, 0.4]$
d_2 (m)	8
n_s	2, 4, 6, 8, 10
n_c	2
Δx (λ)	0.1

sphere. The Rx is assumed with the same height (i.e., x-value) as the center of the sphere. R denotes the radius of the sphere. d_1 denotes the distance between the center of the sphere and the phase center. d_2 denotes the distance between the phase center and the Rx.

Table 4 shows the simulation parameters for a dielectric sphere. Same with Section III, four frequencies are considered. By considering the human-shadowing problem, the relative complex permittivity $\dot{\epsilon}_r$ of the dielectric sphere is set to $11.7 - j14.3$, $8.0 - j10.9$, $6.4 - j8.6$, and $5.6 - j7.1$ for 40 GHz, 60 GHz, 80 GHz, and 100 GHz, respectively [41]. The values of n_s and d_1, the simulation software, and the performance of the calculating computer have been introduced in Section III.

Figures 13a-13d show the plots of the shadowing gain for a dielectric sphere at 40 GHz, 60 GHz, 80 GHz, and 100 GHz, respectively. Similar to Section III, the exact solutions at two polarization and the 3D SSPE/MKA with five n_s-values are simulated for 200 d_1-values at each frequency. The results show that the 3D SSPE/MKA with the proposed parameter $n_s \geq 4$ is a good agreement with the exact solution. Considering the exact solution as a reference, the authors calculate the RMSE in (19), where SG_j^{Ref} is the shadowing gain calculated by the exact solution on a dB scale for the j^{th} test, and SG_j^{Pro} is the shadowing gain calculated by the SSPE/MKA on a dB scale for the j^{th} test. The RMSEs at all the frequencies, polarization, and n_s-values are summarized in Table 5.

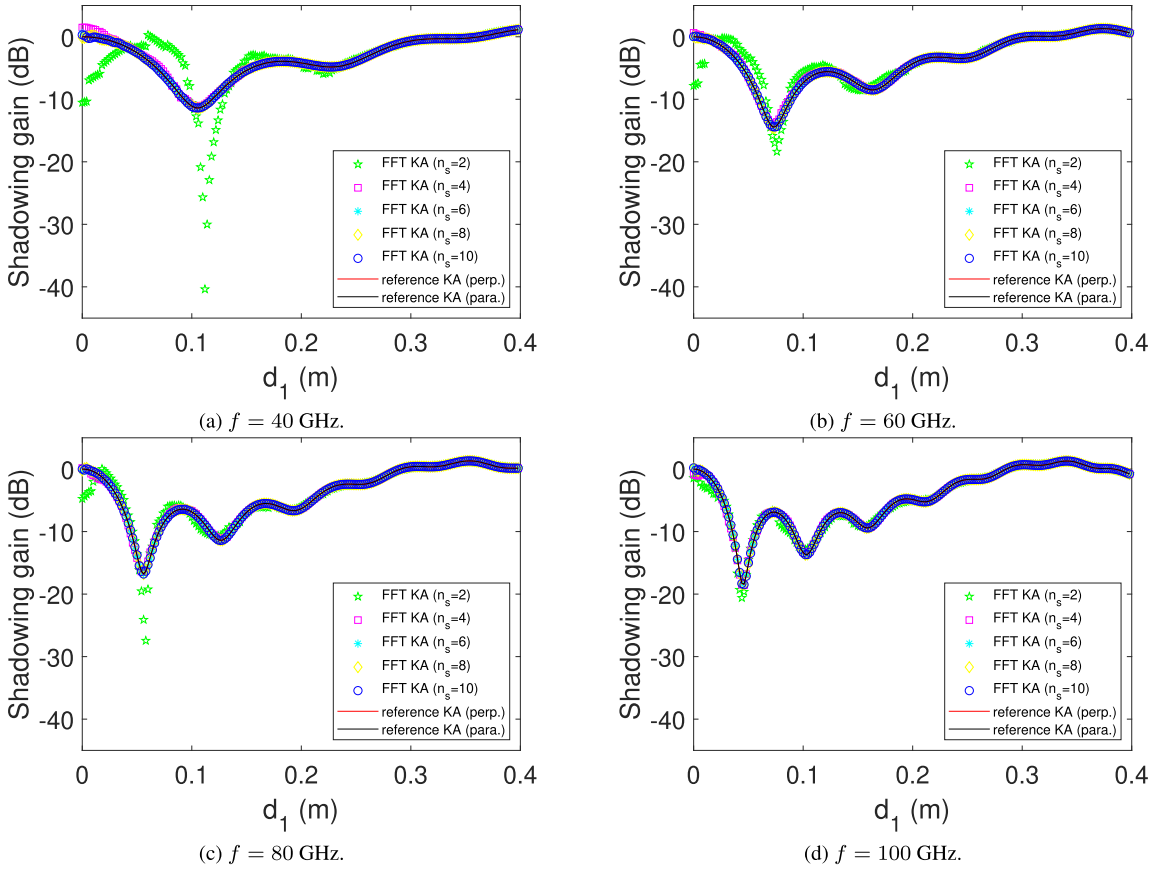

(a) $f = 40$ GHz. (b) $f = 60$ GHz.

(c) $f = 80$ GHz. (d) $f = 100$ GHz.

FIGURE 11. Plots of the shadowing gain for a circular absorber screen.

TABLE 5. Summary of the RMSEs at different frequencies, polarization, and n_s-values for a dielectric sphere.

Frequencies (polarization)	RMSEs at $n_s = 2$	RMSEs at $n_s = 4$	RMSEs at $n_s = 6$	RMSEs at $n_s = 8$	RMSEs at $n_s = 10$
40 GHz (perp.)	7.46 dB	0.70 dB	0.26 dB	0.21 dB	0.19 dB
40 GHz (para.)	7.28 dB	0.89 dB	0.34 dB	0.26 dB	0.24 dB
60 GHz (perp.)	8.29 dB	0.47 dB	0.22 dB	0.19 dB	0.18 dB
60 GHz (para.)	8.16 dB	0.51 dB	0.29 dB	0.26 dB	0.24 dB
80 GHz (perp.)	4.86 dB	0.45 dB	0.20 dB	0.18 dB	0.17 dB
80 GHz (para.)	4.81 dB	0.43 dB	0.26 dB	0.24 dB	0.23 dB
100 GHz (perp.)	5.31 dB	0.37 dB	0.18 dB	0.17 dB	0.16 dB
100 GHz (para.)	5.29 dB	0.43 dB	0.26 dB	0.23 dB	0.21 dB

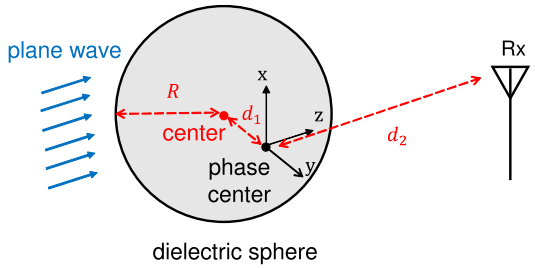

FIGURE 12. Simulation environment for a dielectric sphere.

The results show that the 3D SSPE/MKA with the proposed parameter $n_s \geq 4$ achieves a good accuracy with a low root-mean-square error of less than 1 dB, compared with the exact solution. Thus, the accuracy of the 3D SSPE/MKA with the proposed parameters is validated. The computational time of the SSPE/MKA at all the frequencies and n_s-values are summarized in Table 6. From Table 6, we can conclude that the proposed parameter $n_s = 4$ has a good balance between accuracy and computational time.

V. CONCLUSION

In this paper, the simulation parameters of the 2D FFT including the sampling interval in the angular spectral domain, the truncation size in the space domain, and the windowing functions in the space and angular spectral domains, were proposed for the 3D SSPE/MKA. The validity of the proposed parameters was confirmed for a circular absorber screen at mmWave/THz bands, by using a reference KA. Moreover, the accuracy of the 3D SSPE/MKA with the proposed parameters was validated for a dielectric sphere,

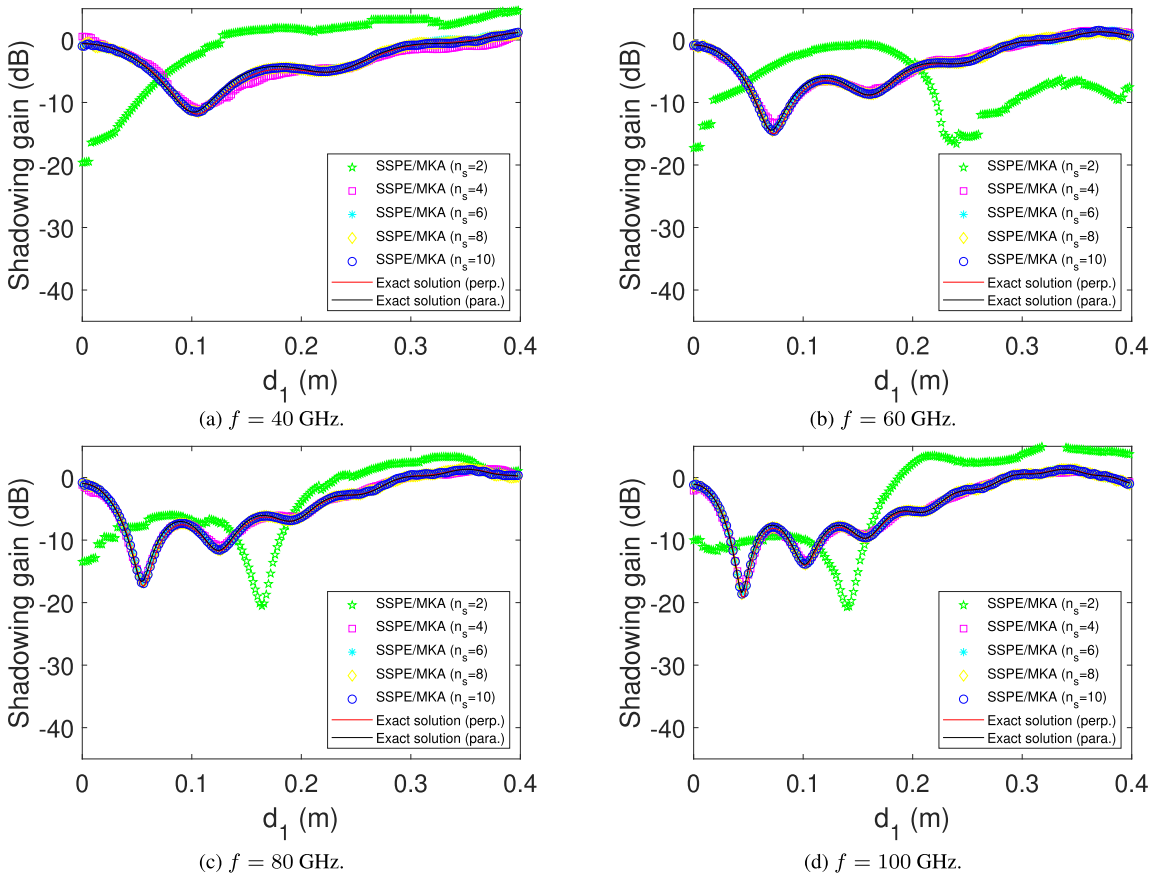

(a) $f = 40$ GHz. (b) $f = 60$ GHz.

(c) $f = 80$ GHz. (d) $f = 100$ GHz.

FIGURE 13. Plots of the shadowing gain for a dielectric sphere.

TABLE 6. Summary of the computational time (Cal. time) of the SSPE/MKA at different frequencies and n_s-values for a dielectric sphere.

Frequencies	Cal. time at $n_s = 2$	Cal. time at $n_s = 4$	Cal. time at $n_s = 6$	Cal. time at $n_s = 8$	Cal. time at $n_s = 10$
40 GHz	0.7 s – 0.9 s	3.0 s – 3.1 s	7.1 s – 7.2 s	12.6 s – 12.7 s	21.7 s – 22.1 s
60 GHz	2.3 s – 2.5 s	10.7 s – 10.8 s	25.1 s – 25.6 s	42.6 s – 42.9 s	69.0 s – 77.1 s
80 GHz	6.0 s – 6.2 s	24.9 s – 25.3 s	56.0 s – 56.5 s	100.8 s – 102.1 s	166.0 s – 167.3 s
100 GHz	11.9 s – 12.4 s	49.9 s – 50.2 s	113.9 s – 126.4 s	208.2 s – 229.7 s	332.6 s – 339.1 s

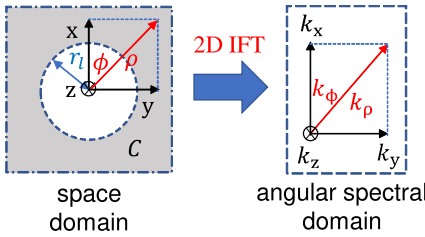

FIGURE 14. Model of the 2D IFT.

by using the exact solution. The results showed that the KA and SSPE/MKA with the proposed parameters presented a good accuracy with a low root-mean-square error of less than 1 dB, compared with the reference KA and the exact solution, respectively. Furthermore, the parameter, which could achieve a good balance between accuracy and computational time, was designed. The application of this work is expected to evaluate the human-shadowing problem more accurately than a ray-based method such as the UTD, which is difficult to handle objects with complex shapes. The limitation of this work is lacking the experimental results. In the future, the measurement of the human-shadowing problem will be conducted to evaluate the SSPE/MKA and UTD further. The comparisons between SSPE/MKA and UTD for objects with complex shapes in terms of accuracy and computational load are future topics.

APPENDIX A DERIVATIONS of the 2D IFT OF THE FIELDS

As shown in Fig. 14, the x-y and k_x-k_y coordinate systems are transferred to the ρ-ϕ and k_ρ-k_ϕ coordinate systems, respectively. Viz.

$$x = \rho \cos\phi \tag{20a}$$
$$y = \rho \sin\phi \tag{20b}$$
$$k_x = k_\rho \cos k_\phi \tag{20c}$$
$$k_y = k_\rho \sin k_\phi \tag{20d}$$

with

$$dxdy = \rho d\rho d\phi \tag{21}$$

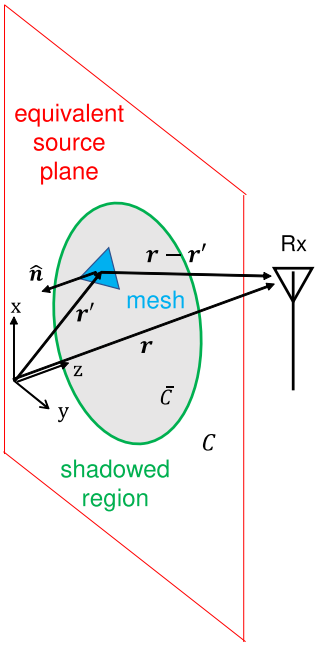

FIGURE 15. Model of the KA.

The surface integral in (5) now reads

$$\iint_C E_l^{\mathrm{i}} e^{\mathrm{j}(k_x x + k_y y)} \mathrm{d}x\mathrm{d}y = E_l^{\mathrm{i}} \int_{r_l}^{\infty} \rho \left\{ \int_0^{2\pi} e^{\mathrm{j}\rho k_\rho \cos(k_\phi - \phi)} \mathrm{d}k_\phi \right\} \mathrm{d}\rho \tag{22}$$

Applying the integral form of the Bessel function of the first kind for the zeroth order as

$$J_0(z) = \frac{1}{2\pi} \int_{\phi}^{2\pi+\phi} e^{-\mathrm{j}z\cos k_\phi} \mathrm{d}k_\phi \tag{23}$$

The integral in (22) now reads

$$E_l^{\mathrm{i}} \int_{r_l}^{\infty} \rho \left\{ \int_0^{2\pi} e^{\mathrm{j}\rho k_\rho \cos(k_\phi - \phi)} \mathrm{d}k_\phi \right\} \mathrm{d}\rho = E_l^{\mathrm{i}} \int_{r_l}^{\infty} \rho \left\{ -2\pi J_0(\rho k_\rho) \right\} \mathrm{d}\rho \tag{24}$$

The formulation of the indefinite integral is applied as

$$\int \rho J_0(\rho k_\rho) \mathrm{d}\rho = \frac{\rho}{k_\rho} J_1(\rho k_\rho) + \text{constant} \tag{25}$$

Finally, the 2D IFT is calculated as

$$E_l^{\mathrm{i}} \int_{r_l}^{\infty} \rho \left\{ -2\pi J_0(\rho k_\rho) \right\} \mathrm{d}\rho = 2\pi E_l^{\mathrm{i}} r_l \frac{J_1(r_l k_\rho)}{k_\rho} \tag{26}$$

by taking the limitation as

$$\lim_{\rho \to \infty} \rho J_1(\rho k_\rho) = 0 \tag{27}$$

APPENDIX B KIRCHHOFF APPROXIMATION

In the KA calculation, the forward scattering is radiated from an equivalent source plane excluding the shadowed region, as shown in Fig. 15. It is more convenient to calculate the scattered field from the shadowed region first and then add it to the incident field, since the integral over the finite area does not need the windowing truncation. The shadowed region is divided into many meshes for numerical integration. $\boldsymbol{r}'$ and $\boldsymbol{r}$ are supposed as the position vectors of the mesh and observation point (Rx), respectively.

By applying the KA, the induced currents generated on the mesh can be approximated as

$$\boldsymbol{J}(\boldsymbol{r}') \approx \hat{\boldsymbol{n}} \times \boldsymbol{H}^{\mathrm{i}}(\boldsymbol{r}') \tag{28}$$

$$\boldsymbol{M}(\boldsymbol{r}') \approx \boldsymbol{E}^{\mathrm{i}}(\boldsymbol{r}') \times \hat{\boldsymbol{n}} \tag{29}$$

where $\boldsymbol{J}(\boldsymbol{r}')$, $\boldsymbol{M}(\boldsymbol{r}')$, $\boldsymbol{E}^{\mathrm{i}}(\boldsymbol{r}')$, and $\boldsymbol{H}^{\mathrm{i}}(\boldsymbol{r}')$ are the induced electric current, induced magnetic current, incident electric field, and incident magnetic field upon the mesh ($\boldsymbol{r}'$), respectively. $\hat{\boldsymbol{n}}$ is the normal vector of the mesh surface.

The vector potentials $\boldsymbol{A}(\cdot)$ and $\boldsymbol{B}(\cdot)$ can be used to determine the field [42] and are calculated as

$$\boldsymbol{A}(\boldsymbol{r}) = \int_{\bar{C}} \boldsymbol{J}(\boldsymbol{r}') G(\boldsymbol{r}, \boldsymbol{r}') \mathrm{d}\boldsymbol{r}' \tag{30}$$

$$\boldsymbol{B}(\boldsymbol{r}) = \int_{\bar{C}} \boldsymbol{M}(\boldsymbol{r}') G(\boldsymbol{r}, \boldsymbol{r}') \mathrm{d}\boldsymbol{r}' \tag{31}$$

where the surface integrals can be calculated by a Ludwig numerical approach [43]. $G(\cdot)$ is the 3D free-space Green function defined as

$$G(\boldsymbol{r}, \boldsymbol{r}') := \frac{e^{-\mathrm{j}k_0 |\boldsymbol{r} - \boldsymbol{r}'|}}{4\pi |\boldsymbol{r} - \boldsymbol{r}'|} \tag{32}$$

By assuming the far-field condition, the scattered field from the shadowed region can be approximated as

$$\boldsymbol{E}^{\mathrm{s}}(\boldsymbol{r}) \approx \mathrm{j}\omega_0 \mu_0 \boldsymbol{A}(\boldsymbol{r}) \times \hat{\boldsymbol{r}} \times \hat{\boldsymbol{r}} - \mathrm{j}\omega_0 \eta_0 \epsilon_0 \boldsymbol{B}(\boldsymbol{r}) \times \hat{\boldsymbol{r}} \tag{33}$$

where ϵ_0, μ_0, ω_0, and η_0 are the permittivity, permeability, angular frequency, and wave impedance in the free space, respectively. $\boldsymbol{E}^{\mathrm{s}}(\boldsymbol{r})$ is the scattered electrical field at the Rx ($\boldsymbol{r}$). $\hat{\boldsymbol{r}}$ is the unit vector of $\boldsymbol{r}$.

Finally, the total field $\boldsymbol{E}^{\mathrm{t}}(\boldsymbol{r})$ at the Rx ($\boldsymbol{r}$) is calculated as

$$\boldsymbol{E}^{\mathrm{t}}(\boldsymbol{r}) = \boldsymbol{E}^{\mathrm{i}}(\boldsymbol{r}) + \boldsymbol{E}^{\mathrm{s}}(\boldsymbol{r}) \tag{34}$$

APPENDIX C EXACT SOLUTIONS OF THE SCATTERING BY A LOSSY DIELECTRIC SPHERE

As shown in Fig. 16, we assume that the electric field of a uniform plane wave polarized in the x direction is incident along the z-axis. The incident electric field upon the point of (r, θ, ϕ) can be expressed as

$$\boldsymbol{E}^{\mathrm{i}} = \hat{x} E_{\mathrm{x}}^{\mathrm{i}} = \hat{x} E_0 e^{-\mathrm{j}k_0 r \cos\theta} \tag{35}$$

where $\hat{x}$, $\hat{y}$, and $\hat{z}$ are the unit vectors of the x, y, and z directions, respectively. r, θ, and ϕ are the parameters of the spherical coordinate system. $E_{\mathrm{x,y,z}}^{\mathrm{i,s}}$ and $E_{\mathrm{r},\theta,\phi}^{\mathrm{i,s}}$ are the electric field components in the rectangular and spherical

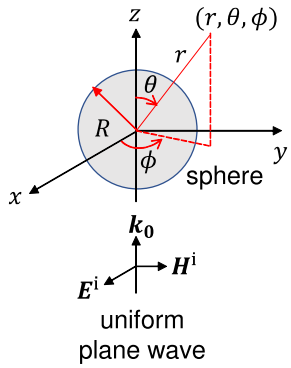

FIGURE 16. Scattering by a sphere.

coordinate systems, respectively. The i, s superscript of E is directly associated with the incident or scattered field. E_0 is the magnitude of the electric field of the source.

The scattered electric field by a dielectric sphere with a radius of R can be derived as

$$E_{\mathrm{r}}^{\mathrm{s}} = -\mathrm{j}E_0\cos\phi\sum_{n=1}^{\infty} b_n\left[\hat{H}_n^{(2)\prime\prime}(k_0 r) + \hat{H}_n^{(2)}(k_0 r)\right]P_n^1(\cos\theta) \tag{36a}$$

$$E_{\theta}^{\mathrm{s}} = \frac{E_0}{k_0 r}\cos\phi\sum_{n=1}^{\infty}\left[\mathrm{j}b_n\hat{H}_n^{(2)\prime}(k_0 r)P_n^{1\prime}(\cos\theta)\sin\theta - c_n\hat{H}_n^{(2)}(k_0 r)\frac{P_n^1(\cos\theta)}{\sin\theta}\right] \tag{36b}$$

$$E_{\phi}^{\mathrm{s}} = \frac{E_0}{k_0 r}\sin\phi\sum_{n=1}^{\infty}\left[\mathrm{j}b_n\hat{H}_n^{(2)\prime}(k_0 r)\frac{P_n^1(\cos\theta)}{\sin\theta} - c_n\hat{H}_n^{(2)}(k_0 r)P_n^{1\prime}(\cos\theta)\sin\theta\right] \tag{36c}$$

with

$$a_n = \mathrm{j}^{-n}\frac{2n+1}{n(n+1)} \tag{37a}$$

$$b_n = a_n\frac{-\sqrt{\frac{\dot{\epsilon}_{\mathrm{r}}}{\dot{\mu}_{\mathrm{r}}}}\hat{J}_n'(k_0R)\hat{J}_n(\dot{k}_{\mathrm{d}}R) + \hat{J}_n(k_0R)\hat{J}_n'(\dot{k}_{\mathrm{d}}R)}{\sqrt{\frac{\dot{\epsilon}_{\mathrm{r}}}{\dot{\mu}_{\mathrm{r}}}}\hat{H}_n^{(2)\prime}(k_0R)\hat{J}_n(\dot{k}_{\mathrm{d}}R) - \hat{H}_n^{(2)}(k_0R)\hat{J}_n'(\dot{k}_{\mathrm{d}}R)} \tag{37b}$$

$$c_n = a_n\frac{-\sqrt{\frac{\dot{\epsilon}_{\mathrm{r}}}{\dot{\mu}_{\mathrm{r}}}}\hat{J}_n(k_0R)\hat{J}_n'(\dot{k}_{\mathrm{d}}R) + \hat{J}_n'(k_0R)\hat{J}_n(\dot{k}_{\mathrm{d}}R)}{\sqrt{\frac{\dot{\epsilon}_{\mathrm{r}}}{\dot{\mu}_{\mathrm{r}}}}\hat{H}_n^{(2)}(k_0R)\hat{J}_n'(\dot{k}_{\mathrm{d}}R) - \hat{H}_n^{(2)\prime}(k_0R)\hat{J}_n(\dot{k}_{\mathrm{d}}R)} \tag{37c}$$

where $\dot{\epsilon}_{\mathrm{r}}$ and $\dot{\mu}_{\mathrm{r}}$ are the relative complex permittivity and permeability, respectively. The real and imaginary parts of $\dot{\epsilon}_{\mathrm{r}}$ correspond to the relative permittivity and conductivity, respectively. $\dot{k}_{\mathrm{d}}$ is the complex wave number in the dielectric sphere [42].

The functions $\hat{J}_n(\cdot)$, $\hat{H}_n^{(2)}(\cdot)$, and $P_n^m(\cdot)$ are defined as

$$\hat{J}_n(x) := xj_n(x) \tag{38a}$$

$$\hat{H}_n^{(2)}(x) := xh_n^{(2)}(x) \tag{38b}$$

$$P_n^m(x) := (-1)^m(1-x^2)^{m/2}\frac{\mathrm{d}^m P_n(x)}{\mathrm{d}x^m} \tag{38c}$$

where $j_n(\cdot)$, $h_n^{(2)}(\cdot)$, and $P_n(\cdot)$ are the spherical Bessel function of the first kind, the spherical Hankel function of the second kind, and the Legendre function of the first kind, respectively, for the n^{th} order. The derivatives of those functions in (36)-(37) are defined as

$$\hat{H}_n^{(2)\prime}(k_0 r) := \frac{\partial}{\partial(k_0 r)}\hat{H}_n^{(2)}(k_0 r) \tag{39a}$$

$$\hat{H}_n^{(2)\prime\prime}(k_0 r) := \frac{\partial^2}{\partial(k_0 r)^2}\hat{H}_n^{(2)}(k_0 r) \tag{39b}$$

$$\hat{J}_n'(k_0 r) := \frac{\partial}{\partial(k_0 r)}\hat{J}_n(k_0 r) \tag{39c}$$

$$P_n^{1\prime}(\cos\theta) := -\frac{1}{\sin\theta}\frac{\partial}{\partial\theta}P_n^1(\cos\theta) \tag{39d}$$

Note that either $P_n^1(\cos\theta)/\sin\theta$ or $P_n^{1\prime}(\cos\theta)\sin\theta$ in (36) has the singularities at $\theta = 0$ and $\theta = \pi$. The values at $\theta = 0$ and $\theta = \pi$ are defined to be the limiting values as

$$\lim_{\theta\to 0}\frac{P_n^1(\cos\theta)}{\sin\theta} = -\frac{n(n+1)}{2} \tag{40a}$$

$$\lim_{\theta\to \pi}\frac{P_n^1(\cos\theta)}{\sin\theta} = (-1)^n\frac{n(n+1)}{2} \tag{40b}$$

$$\lim_{\theta\to 0}P_n^{1\prime}(\cos\theta)\sin\theta = \frac{n(n+1)}{2} \tag{40c}$$

$$\lim_{\theta\to \pi}P_n^{1\prime}(\cos\theta)\sin\theta = (-1)^n\frac{n(n+1)}{2} \tag{40d}$$

The scattered electric field components in the rectangular coordinate system can be obtained by the spherical-to-rectangular transformation as

$$\begin{pmatrix}E_{\mathrm{x}}^{\mathrm{s}}\\ E_{\mathrm{y}}^{\mathrm{s}}\\ E_{\mathrm{z}}^{\mathrm{s}}\end{pmatrix} = \begin{pmatrix}\sin\theta\cos\phi & \cos\theta\cos\phi & -\sin\phi\\ \sin\theta\sin\phi & \cos\theta\sin\phi & \cos\phi\\ \cos\theta & -\sin\theta & 0\end{pmatrix}\begin{pmatrix}E_{\mathrm{r}}^{\mathrm{s}}\\ E_{\theta}^{\mathrm{s}}\\ E_{\phi}^{\mathrm{s}}\end{pmatrix} \tag{41}$$

Finally, the scattered field $\boldsymbol{E}^{\mathrm{s}}$ and total field $\boldsymbol{E}^{\mathrm{t}}$ are calculated by (42) and (43), respectively.

$$\boldsymbol{E}^{\mathrm{s}} = \hat{x}E_{\mathrm{x}}^{\mathrm{s}} + \hat{y}E_{\mathrm{y}}^{\mathrm{s}} + \hat{z}E_{\mathrm{z}}^{\mathrm{s}} \tag{42}$$

$$\boldsymbol{E}^{\mathrm{t}} = \boldsymbol{E}^{\mathrm{i}} + \boldsymbol{E}^{\mathrm{s}} \tag{43}$$

REFERENCES

[1] D. E. Freund, N. E. Woods, H.-C. Ku, and R. S. Awadallah, "Forward radar propagation over a rough sea surface: A numerical assessment of the Miller-Brown approximation using a horizontally polarized 3-GHz line source," *IEEE Trans. Antennas Propag.*, vol. 54, no. 4, pp. 1292–1304, Apr. 2006.

[2] G. D. Dockery, R. S. Awadallah, D. E. Freund, J. Z. Gehman, and M. H. Newkirk, "An overview of recent advances for the TEMPER radar propagation model," in *Proc. IEEE Radar Conf.*, Apr. 2007, pp. 896–905.

[3] J. I. Glaser, "Bistatic RCS of complex objects near forward scatter," *IEEE Trans. Aerosp. Electron. Syst.*, vol. AES-21, no. 1, pp. 70–78, Jan. 1985.

[4] G. R. MacCartney, S. Deng, S. Sun, and T. S. Rappaport, "Millimeter-wave human blockage at 73 GHz with a simple double knife-edge diffraction model and extension for directional antennas," in *Proc. IEEE 84th Veh. Technol. Conf. (VTC-Fall)*, Montreal, QC, Canada, Sep. 2016, pp. 1–6.

[5] J. G. Andrews, S. Buzzi, W. Choi, S. V. Hanly, A. Lozano, A. C. K. Soong, and J. C. Zhang, "What will 5G be?" *IEEE J. Sel. Areas Commun.*, vol. 32, no. 6, pp. 1065–1082, Jun. 2014.

[6] S. Rangan, T. S. Rappaport, and E. Erkip, "Millimeter-wave cellular wireless networks: Potentials and challenges," *Proc. IEEE*, vol. 102, no. 3, pp. 366–385, Mar. 2014.

[7] T. S. Rappaport, Y. Xing, O. Kanhere, S. Ju, A. Madanayake, S. Mandal, A. Alkhateeb, and G. C. Trichopoulos, "Wireless communications and applications above 100 GHz: Opportunities and challenges for 6G and beyond," *IEEE Access*, vol. 7, pp. 78729–78757, 2019.
[8] S. Sun, T. S. Rappaport, R. W. Heath Jr., A. Nix, and S. Rangan, "MIMO for millimeter-wave wireless communications: Beamforming, spatial multiplexing, or both?" *IEEE Commun. Mag.*, vol. 52, no. 12, pp. 110–121, Dec. 2014.
[9] S. Sun, G. R. MacCartney, M. K. Samimi, and T. S. Rappaport, "Synthesizing omnidirectional antenna patterns, received power and path loss from directional antennas for 5G millimeter-wave communications," in *Proc. IEEE Global Commun. Conf. (GLOBECOM)*, Dec. 2015, pp. 3948–3953.
[10] Z. J. Csendes and P. Silvester, "Numerical solution of dielectric loaded waveguides: I-finite-element analysis," *IEEE Trans. Microw. Theory Techn.*, vol. MTT-18, no. 12, pp. 1124–1131, Dec. 1970.
[11] R. F. Harrington, *Field Computation by Moment Method*. New York, NY, USA: Macmillan, 1968, pp. 1–6.
[12] W. C. Chew, J. M. Jin, E. Michielssen, and J. Song, *Fast and Efficient Algorithms in Computational Electromagnetic*. Boston, MA, USA: Artech House, 2001.
[13] K. Yee, "Numerical solution of initial boundary value problems involving Maxwell's equations in isotropic media," *IEEE Trans. Antennas Propag.*, vol. AP-14, no. 3, pp. 302–307, May 1966.
[14] R. G. Kouyoumjian and P. H. Pathak, "A uniform geometrical theory of diffraction for an edge in a perfectly conducting surface," *Proc. IEEE*, vol. 62, no. 11, pp. 1448–1461, Nov. 1974.
[15] P. Pathak, W. Burnside, and R. Marhefka, "A uniform GTD analysis of the diffraction of electromagnetic waves by a smooth convex surface," *IEEE Trans. Antennas Propag.*, vol. AP-28, no. 5, pp. 631–642, Sep. 1980.
[16] P. H. Pathak, "An asymptotic analysis of the scattering of plane waves by a smooth convex cylinder," *Radio Sci.*, vol. 14, no. 3, pp. 419–435, May 1979.
[17] P. Y. Ufimtsev, "New insight into the classical Macdonald physical optics approximation," *IEEE Antennas Propag. Mag.*, vol. 50, no. 3, pp. 11–20, Jun. 2008.
[18] K. Hentschel, N. Y. Zhu, and G. R. K. Treatise, *Gustav Robert Kirchhoff's Treatise 'On the Theory of Light Rays' (1882) English Translation, Analysis and Commentary*. Singapore: World Scientific, 2017.
[19] C. A. Balanis, *Antenna Theory*. Hoboken, NJ, USA: Wiley, 2016, pp. 620–637.
[20] P. T. C. Lam, S. W. Lee, and R. Acosta, *Secondary Pattern Computation of an Arbitrarily Shaped Main Reflector*. Cleveland, OH, USA: Lewis Research Center, Nov. 1984.
[21] D. Comite, M. T. Falconi, P. Lombardo, F. S. Marzano, and A. Galli, "Investigating the shadow radiation of 3-dimensional radar targets in the near field," in *Proc. Eur. Radar Conf. (EURAD)*, Oct. 2017, pp. 17–20.
[22] P. Y. Ufimtsev, *Fundamentals of the Physical Theory of Diffraction*. Hoboken, NJ, USA: Wiley, 2013, pp. 1–48.
[23] X. Du, K. Saito, J.-I. Takada, and P. Hanpinitsak, "A novel mirror Kirchhoff approximation method for predicting the shadowing effect by a metal cuboid," *Prog. Electromagn. Res. M*, vol. 104, pp. 199–212, 2021.
[24] X. Du and J. Takada, "Mirror Kirchhoff approximation for predicting shadowing effect by a PEC convex cylinder," in *Proc. Appl. Computa. Electromagn. Soci.*, Aug. 2021, pp. 1–3.
[25] M. Levy, *Parabolic Equation Methods for Electromagnetic Wave Propagation*. London, U.K.: IET, Jan. 2000, p. 184.
[26] A. E. Barrios, "A terrain parabolic equation model for propagation in the troposphere," *IEEE Trans. Antennas Propag.*, vol. 42, no. 1, pp. 90–98, Jan. 1994.
[27] G. Apaydin and L. Sevgi, *Radio Wave Propagation and Parabolic Equation Modeling*. Hoboken, NJ, USA: Wiley, 2017.
[28] M. D. Feit and J. A. Fleck, "Calculation of dispersion in graded-index multimode fibers by a propagating-beam method," *Appl. Opt.*, vol. 18, no. 16, pp. 2843–2851, Aug. 1979.
[29] X. Du and J.-I. Takada, "Low computational cost mirror Kirchhoff approximation for predicting shadowing effect," *IEEE Access*, vol. 10, pp. 23829–23841, 2022.
[30] F. J. Harris, "On the use of windows for harmonic analysis with the discrete Fourier transform," *Proc. IEEE*, vol. 66, no. 1, pp. 51–83, Jan. 1978.
[31] H. Hu, Z. Chen, S. Chai, and J. Mao, "Research on mobile communication radio propagation characteristic based on 3DPE," in *Proc. Asia–Pacific Microw. Conf. Proc.*, Hong Kong, 2005, p. 3.
[32] P. Zhang, L. Bai, Z. Wu, and F. Li, "Effect of window function on absorbing layers top boundary in parabolic equation," in *Proc. 3rd Asia–Pacific Conf. Antennas Propag.*, Harbin, China, Jul. 2014, pp. 849–852.
[33] H. F. Rasool, X.-M. Pan, and X.-Q. Sheng, "Radiowave propagation prediction in the presence of multiple knife edges using 3D parabolic equation method," in *Proc. Int. Appl. Comput. Electromagn. Soc. Symp.*, Jul. 2018, pp. 1–2.
[34] L. Guo and X. Guan, "A vector parabolic equation method for propagation predictions over 3-D irregular terrains," in *Proc. IEEE Int. Conf. Comput. Electromagn. (ICCEM)*, Mar. 2018, pp. 1–4.
[35] T. Kohama and M. Ando, "Localization of radiation integrals using the Fresnel zone numbers," *IEICE Trans. Electron.*, vol. 95, no. 5, pp. 928–935, 2012.
[36] T. Kohama and M. Ando, "Physical optics radiation integrals with frequency-independent number of division utilizing Fresnel zone number localization and adaptive sampling method," *IEICE Trans. Electron.*, vol. 97, no. 12, pp. 1134–1141, 2014.
[37] M. Ali, T. Kohama, and M. Ando, "Modified edge representation (MER) consisting of Keller's diffraction coefficients with weighted fringe waves and its localization for evaluation of corner diffraction," *IEEE Trans. Antennas Propag.*, vol. 63, no. 7, pp. 3158–3167, Jul. 2015.
[38] A. B. Katrich, "On the propagation of evanescent waves," in *Proc. 4th Int. Conf. Adv. Optoelectron. Lasers*, Sep. 2008, pp. 304–306.
[39] W. H. Southwell, "Validity of the Fresnel approximation in the near field," *J. Opt. Soc. Amer.*, vol. 71, no. 1, pp. 7–14, 1981.
[40] X. Du and J.-I. Takada, "Structure of the field behind a dielectric circular cylinder in the lit side of the transition region," *Prog. Electromagn. Res. M*, vol. 116, pp. 103–118, 2023.
[41] T. Wu, T. S. Rappaport, and C. M. Collins, "The human body and millimeter-wave wireless communication systems: Interactions and implications," in *Proc. IEEE Int. Conf. Commun. (ICC)*, London, U.K., Jun. 2015, pp. 2423–2429.
[42] C. A. Balanis, *Advanced Engineering Electromagnetics*. Hoboken, NJ, USA: Wiley, 2012.
[43] A. Ludwig, "Computation of radiation patterns involving numerical double integration," *IEEE Trans. Antennas Propag.*, vol. AP-16, no. 6, pp. 767–769, Nov. 1968.

XIN DU (Member, IEEE) was born in 1992. He received the B.E. degree in international development engineering and the M.S. and D.E. degrees in transdisciplinary science and engineering from the Tokyo Institute of Technology, Tokyo, Japan, in 2017, 2019, and 2022, respectively.

From 2017 to 2019, he was a Research Assistant with the School of Environment and Society, Tokyo Institute of Technology. He is currently a Postdoctoral Researcher with the Tokyo Institute of Technology. His research interests include numerical electromagnetic simulation, diffraction theory, and reconfigurable intelligent surfaces.

Dr. Du is a member of the IEICE, Japan.

JUN-ICHI TAKADA (Senior Member, IEEE) received the B.E., M.E., and D.E. degrees in electrical and electronic engineering from the Tokyo Institute of Technology, Tokyo, Japan, in 1987, 1989, and 1992, respectively.

He was a Research Associate with Chiba University, Chiba, Japan, from 1992 to 1994, an Associate Professor with the Tokyo Institute of Technology, from 1994 to 2006, and a Researcher with the National Institute of Information and Communications Technology, Kanagawa, Japan, from 2003 to 2007. Since 2006, he has been a Professor with the Tokyo Institute of Technology. His research interests include radio-wave propagation and channel modeling for mobile and short-range wireless systems, regulatory issues of spectrum sharing, and ICT applications for international development.

Dr. Takada is a fellow of the IEICE, Japan.